A Variable-Density Fictitious-Domain Method for Fully Resolved Simulation of High-Density Ratio Fluid-Particle Systems

Sourabh V. Apte* and Justin Finn*

* School of Mechanical Industrial and Manufacturing Engineering

Oregon State University, Corvallis, OR 97333, USA

sva@engr.orst.edu and finnj@engr.orst.edu

Keywords: Fully resolved simulations, fictitious domain methods, high-density ratio,

freely moving particles, particle-vortex interactions.

Abstract

A numerical scheme for fully resolved simulation of fluid-particle systems with freely moving rigid particles is developed. The approach is based on a fictitious domain method wherein the entire fluid-particle domain is assumed to be an incompressible fluid but with variable density. The flow inside the particle domain is constrained to be a rigid body motion using an additional rigidity constraint in a fractional step scheme. The rigidity constraint force is obtained based on the fast computation technique proposed by Sharma and Patankar (2005). The particle is assumed to be made up of material points moving on a fixed background mesh where the fluid flow equations are solved. The basic finite-volume solver is based on a co-located grid incompressible but variable density flow. The incompressibility constraint is imposed by solving a variable-coefficient pressure equation giving rise to a stable scheme for high density ratio fluid-particle systems. Through various verification and validation test cases on fixed and freely moving particles it is shown that the numerical approach is accurate and stable for a wide range of fluid-particle density ratios.

Introduction

Fully resolved simulations (FRS) of fluid-particle systems, wherein all scales associated with the fluid and particle motion are completely resolved, are of great importance for understanding particle-turbulence interactions. Considerable work has been done on fully resolved simulations of freely moving particles in fluid flows on fixed grids. For example, distributed Lagrange multiplier/fictious domain (DLM) based methods (Glowinski et al. (2001)) and Immersed Boundary method (IBM by Peskin (2003); Mittal and Iaccarino (2005); Uhlmann (2005); Kim and Choi (2006); Mittal et al. (2008)) have been developed and shown to be very effective in computing fluid-particle systems and fluid-structure interaction problems. Lattice Boltzmann method (LBM by Ladd and Verberg (2001)) has been developed and effectively used for simulations of rigid as well as deforming particles. Combination of the DLM, direct forcing based IBM, and Lattice-Boltzmann methods (termed as *Proteus*) was recently developed by Feng and Michaelides (2005). A second-order accurate fixed grid method (PHYSALIS) was developed

by Zhang and Prosperetti (2005), which gives good solutions for *spherical* particles by using local spectral representations of the solution near a spherical boundary.

Taira and Colonius (2007) proposed a new implementation of the immersed boundary method to achieve second-order accuracy. They compared IBM with fictitious-domain based methods to point out subtle differences when the immersed objects are constrained to undergo specified motion. In the fictitious domain/DLM method (see Glowinski et al. (2001); Patankar et al. (2000)), the entire fluid–particle domain is assumed to be a fluid and the flow in the particle domain is constrained to be a rigid-body motion through rigidity constraint in terms of a stress or a force. Sharma and Patankar (2005) proposed a fast technique to obtain the rigidity constraint force that eliminated the need for an iterative procedure to solve for the rigid body motion. Recently, Veeramani et al. (2007) proposed a similar approach in the context of finite-element methods. Apte et al. (2009) extended the finite-volume based fictitious domain approach by Sharma and Patankar (2005) to large number of particles in complex turbulent flows

on co-located grids.

Majority of the above studies have been applied to simulate rigid particulate flows with fluid particle density ratios in the range of $0.1 - 10$. Large density ratios are common in many practical applications involving complex flows; for example coal particles in a oxy-coal boiler, aeolian particle transport, aerosol transport, among others. Being able to simulate such flows with fully resolved direct or large-eddy simulations is critical. The fictitious domain approach with fast computation of the rigidity constraint (Sharma and Patankar (2005); Apte et al. (2009)) when applied to large density ratio fluid-particle systems leads to numerical difficulties. Sharp gradients in density across the fluid-particle interface can cause numerical 'ringing' of the solution. In the present work, we extend this numerical approach to account for fluid-particle systems over a range of density ratios.

The paper is arranged as follows. A mathematical formulation of the fictitious domain scheme is first described. Numerical issues with the original formulation for high density ratios and potential remedies are discussed next. The new approach is implemented in a co-located grid finite volume method. The approach is first validated for basic test cases to show good predictive capability. Namely, flow over a fixed sphere and a NACA hydrofoil are first investigated. Next, freely falling/rising spherical particles at different Reynolds numbers are considered and compared with available experimental data at low fluid-particle density ratios. Finally, the approach is applied to a wide range of density ratios $10^{-3} - 10^6$ to show stable solution. Specifically, interactions of a buoyant sphere with a stationary Gaussian vortex are simulated to show the capability of the approach to study particle-vortex interactions.

Mathematical Formulation

Let Γ be the computational domain which includes both the fluid ($\Gamma_F(t)$) and the particle ($\Gamma_P(t)$) domains. Let the fluid boundary not shared with the particle be denoted by $\mathcal{B}$ and have a Dirichlet condition (generalization of boundary conditions is possible). For simplicity, let there be a single rigid object in the domain and the body force be assumed constant so that there is no net torque acting on the object. The basis of fictitious-domain based approach is to extend the Navier-Stokes equations for fluid motion over the entire domain Γ inclusive of immersed object. The natural choice is to assume that the immersed object region is filled with a Newtonian *fluid* of density equal to the object density (ρ_P) and some fluid viscosity (μ_F). Both the real and fictitious fluid regions will be assumed as incompressible and thus incompressibility constraint applies over

the entire region. In the numerical approach presented by Sharma and Patankar (2005), the particle region is identified by an indicator (color) function Θ which has unit value inside the particle region and vanishes in the fluid region. Owing to finite number of grid cells, the boundary region of the particle typically is smeared with $0 \leq \Theta \leq 1$. The density field over the entire domain is then given as,

$$\rho = \rho_P \Theta + \rho_F (1 - \Theta). \tag{1}$$

The indicator function moves with the particle resulting in

$$\frac{D\Theta}{Dt} = 0, \tag{2}$$

where D/Dt is the material derivative. The fluid velocity field is constrained by the conservation of mass over the entire domain given as

$$\frac{\partial \rho}{\partial t} + \nabla \cdot (\rho \mathbf{u}) = 0. \tag{3}$$

The conservation of mass together with the indicator function advection implies that for an incompressible fluid, $\nabla \cdot \mathbf{u} = 0$ over the entire domain.

The momentum equation for fluid motion applicable in the entire domain Γ in the conservative form is then given by:

$$\frac{\partial \rho \mathbf{u}}{\partial t} + \nabla \cdot (\rho \mathbf{u} \mathbf{u}) = -\nabla p +$$
$$\nabla \cdot \left(\mu_F \left(\nabla \mathbf{u} + (\nabla \mathbf{u})^T \right) \right) + \rho \mathbf{g} + \mathbf{f}, \tag{4}$$

where ρ is the density field, $\mathbf{u}$ the velocity vector, p the pressure, μ_F the fluid viscosity, $\mathbf{g}$ the gravitational acceleration, and $\mathbf{f}$ is an additional body force that enforces rigid body motion within the immersed object region Γ_P. This can be done by following the fast procedure for obtaining the rigidity constraint force as first proposed by Sharma and Patankar (2005) for freely moving rigid objects in laminar flows.

Sharp variations in density over a single grid cell can lead to numerical instabilities when the momentum and continuity equations are solved in the above conservative form. This was shown to be a problem in volume of fluid formulations for two immiscible fluids by Rudman (1998). This problem is remedied by performing consistent flux constructions for mass and momentum fluxes at the control volume faces as shown by Rudman (1998); Bussmann et al. (2002); Raessi (2008). Inconsistencies in flux calculations for mass and momentum leads to incorrect accelerations of fluids near interfaces leading to numerical instability at high density ratios.

An alternative approach, that is commonly followed in interface tracking schemes based on level set methods (Osher and Fedkiw (2003); Osher and Sethian

(1988)), is to solve the above equations in a non-conservative form, wherein computation of density variations across cell faces are not required especially for co-located grid formulations. However, level set methods suffer from the loss of mass owing to the non-conservative advection of the signed-distance function especially for deforming interfaces. For the present work on rigid body motion, the surface area of the interface between the fluid and particles remains constant over time as interface deformation is not possible. Since the rigid particles are advanced in a purely Lagrangian frame their mass is conserved discretely in a numerical formulation. When cast in the non-conservative form, and making use of the fact that the fluid velocity is divergence free over the entire domain, the momentum conservation equation becomes,

$$\frac{\partial \mathbf{u}}{\partial t} + \mathbf{u} \cdot \nabla (\mathbf{u}) = -\frac{1}{\rho} \nabla p +$$
$$\frac{1}{\rho} \nabla \cdot \left(\mu_F \left(\nabla \mathbf{u} + (\nabla \mathbf{u})^T \right) \right) + \mathbf{g} + \frac{1}{\rho} \mathbf{f}. \qquad (5)$$

In the present work, we solve the momentum equation in the above form together with the incompressibility constraint $\nabla \cdot \mathbf{u} = 0$ over the entire domain. In order to enforce that the material inside the immersed object moves in a rigid fashion, a rigidity constraint force is required that leads to a non-zero forcing function $\mathbf{f}$. This can be obtained using a fractional step scheme:

1. In this first step, the rigidity constraint force $\mathbf{f}$ in equation 5 is set to zero and the equation together with the incompressibility constraint is solved by standard fractional-step schemes over the entire domain. Accordingly, a *variable coefficient* pressure Poisson equation is derived and used to project the velocity field onto an incompressible solution. The obtained velocity field is denoted as $\mathbf{u}^{n+1}$ inside the fluid domain and $\hat{\mathbf{u}}$ inside the object.

2. The velocity field for a freely moving object is obtained in a second step by projecting the flow field onto a rigid body motion. Inside the object:

$$\rho_P \left(\frac{\mathbf{u}^{n+1} - \hat{\mathbf{u}}}{\Delta t} \right) = \mathbf{f}. \qquad (6)$$

To solve for $\mathbf{u}^{n+1}$ inside the particle region we require $\mathbf{f}$. This is obtained by first finding the rigid body motion inside the particle region. The velocity field in the particle domain involves only translation and angular velocities. Thus $\hat{\mathbf{u}}$ is split into a rigid body motion ($\mathbf{u}^{RBM} = \mathbf{U} + \Omega \times \mathbf{r}$) and residual non-rigid motion ($\mathbf{u}'$). The translational and rotational components of the rigid body motion are obtained by conserving the linear and angular momenta and are given as:

$$M_P \mathbf{U} = \int_{\Gamma_P} \rho_P \hat{\mathbf{u}} d\mathbf{x}; \qquad (7)$$

$$\mathcal{I}_P \Omega = \int_{\Gamma_P} \mathbf{r} \times \rho_P \hat{\mathbf{u}} d\mathbf{x}, \qquad (8)$$

where M_P is the mass of the particle and $\mathcal{I}_P = \int_{\Gamma_P} \rho_P [(\mathbf{r} \cdot \mathbf{r})\mathbf{I} - \mathbf{r} \otimes \mathbf{r}] d\mathbf{x}$ is the moment of inertia tensor. Knowing $\mathbf{U}$ and Ω for each particle, the rigid body motion inside the particle region $\mathbf{u}^{RBM}$ can be calculated.

3. The rigidity constraint force is then simply obtained as $\mathbf{f} = \rho(\mathbf{u}^{RBM} - \hat{\mathbf{u}})/\Delta t$. This sets $\mathbf{u}^{n+1} = \mathbf{u}^{RBM}$ in the particle domain. Note that the rigidity constraint is non-zero only inside the particle domain and zero everywhere else. This constraint is then imposed in a third fractional step.

Numerical Approach

The preceding mathematical formulation is implemented in a co-located, structured grid, three-dimensional flow solver based on a fractional-step scheme developed by Apte et al. (2009). Accordingly, in the present work the fluid-particle system is solved by a *three-level fractional step scheme*. First the momentum equations (without the pressure and the rigidity constraint terms) are solved. The incompressibility constraint is then imposed by solving a *variable-coefficient Poisson equation* for pressure. Finally, the rigid body motion is enforced by constraining the flow inside the immersed object to translational and rotational motion. The main steps of the numerical approach are given below.

Immersed Object Representation In the numerical implementation, we create small material volumes of cubic shape that completely occupy the immersed object. Each material volume is assigned the properties of the immersed object (e.g. density etc.). The shape of the object can be reconstructed from these material volumes by computing an indicator or color function (with value of unity inside the object and zero outside) on a fixed background mesh used for flow solution. In this work, the material volumes are forced to undergo rigid motion, based on the translational and rotational velocities of the object, resulting in no relative motion among them. At each time-step the material volumes are advanced to new locations. In the present approach, the boundary of the object is represented in a stair-stepped fashion and it is straightforward to create the material volumes using a bounding-box algorithm as described in Apte et al. (2009).
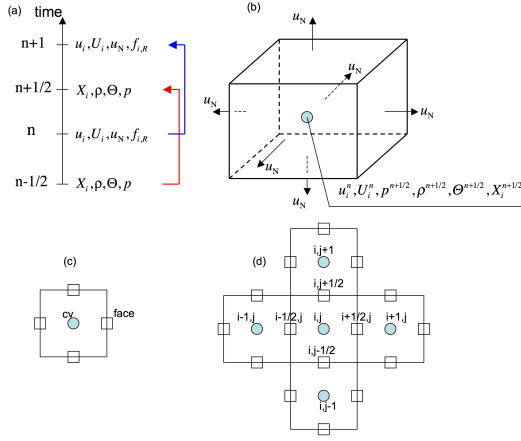
Figure 1: Schematic of the variable storage in time and space: (a) time-staggering, (b) three-dimensional variable storage, (c) cv and face notation, (d) index notation for a given k-index in the z direction. The velocity fields (u_i, u_N) are staggered in time with respect to the volume fraction (Θ), density (ρ), and particle position (X_i), the pressure field (p), and the rigid body force $(f_{i,R})$. All variables are collocated in space at the centroid of a control volume except the face-normal velocity u_N which is stored at the centroid of the faces of the control volume.

Discretized Equations and Numerical Algorithm

Figure 1 shows the schematic of variable storage in time and space. All variables are stored at the control volume (cv) center with the exception of the face-normal velocity u_N, located at the face centers. The face-normal velocity is used to enforce continuity equation. Capital letters are used to denote particle fields. The time-staggering is done so that the variables are located most conveniently for the time-advancement scheme. We follow the collocated spatial arrangement for velocity and pressure field (Kim and Choi (2000), Mahesh et al. (2006)). Accordingly, the particle positions (X_i), density (ρ), volume fraction (Θ), viscosity (μ), and the pressure (p) are located at time level $t^{n-1/2}$ and $t^{n+1/2}$ whereas the velocity fields $(u_i, u_N, \text{ and } U_i)$ and the rigid body constraint force $f_{i,R}$, are located at time level t^n and t^{n+1}. This makes the discretization symmetric in time, a feature important to obtain good conservation properties. The semi-discretization of the governing equations in each time-step is given below.

Step 1: Starting with a solution at t^n and $t^{n-1/2}$, the centroids of material volumes $(X_{i,M})$ representing immersed objects are first advanced explicitly.

$$X_{i,M}^{n+1/2} = X_{i,P}^{n-1/2} + \mathcal{R}_{ij}\left(X_{j,M}^{n-1/2} - X_{j,P}^{n-1/2}\right) + U_{i,M}^n \Delta t, \quad (9)$$

where $X_{i,M}$ is the position vector of the material volume center, $X_{i,P}$ is the position vector of the immersed object centroid, $U_{i,M}$ is the translation velocity, $\Omega_{i,M}$ is the angular velocity, and Δt is the time-step. Here $\mathcal{R}_{ij}$ is the rotation matrix evaluated using particle locations at $t^{n-1/2}$. The details of the particle update and the rotation matrix are similar to that presented by Apte et al. (2009).

Step 2: Knowing the new positions of the material volumes and particle centroid, an indicator function (color function) $\Theta^{n+1/2}$ is evaluated at the cv-center of the fixed background grid. We use a discrete delta-function developed by Roma et al. (1999) to compute the color function. The color function is unity inside the particle region and vanishes outside with smooth variation near the boundary. This thus allows identification of the particle on the background mesh. Details of the interpolation between the material volume centers and the cv center are similar to that presented by Apte et al. (2009). The density and the viscosity are then calculated over the entire domain as:

$$\rho_{cv}^{n+1/2} = \rho_P \Theta_{cv}^{n+1/2} + \rho_F\left(1 - \Theta_{cv}^{n+1/2}\right) \quad (10)$$

$$\mu_{cv}^{n+1/2} = \mu_P \Theta_{cv}^{n+1/2} + \mu_F\left(1 - \Theta_{cv}^{n+1/2}\right) \quad (11)$$

where ρ_P is the density of the immersed particle and ρ_F is the density of the surrounding fluid. Likewise μ_P is dynamic viscosity of the fictitious fluid inside the particle region, and μ_F is the dynamic viscosity of the surrounding fluid. For particles with specified motion (microvalves) μ_P is assumed equal to the fluid viscosity (μ_F).

Step 3: Advance the momentum equations using the fractional step method. First, obtain a predicted velocity field over the entire domain. We advance the velocity field from t^n to t^{n+1}. The predicted velocity fields may not satisfy the continuity or the rigidity constraints. These are enforced later.

$$\frac{u_{i,cv}^* - u_{i,cv}^n}{\Delta t} + \frac{1}{V_{cv}} \sum_{\text{faces of } cv} u_{i,\text{face}}^{*n+1/2} u_N^n A_{\text{face}} =$$

$$\frac{1}{\rho_{cv}^{n+1/2}}\left(\frac{1}{V_{cv}} \sum_{\text{faces of } cv} \tau_{ij,\text{face}}^{*n+1/2} N_{j,\text{face}} A_{\text{face}}\right) + g_i \quad (12)$$

where g_i is the gravitational acceleration, V_{cv} is the volume of the cv, A_{face} is the area of the face of a control volume, $N_{j,\text{face}}$ is the face-normal vector and

$$u_{i,\text{face}}^{*n+1/2} = \frac{1}{2}\left(u_{i,\text{face}}^n + u_{i,\text{face}}^*\right);$$

$$\tau_{ij,\text{face}}^{*n+1/2} = \mu_{cv}^{n+1/2}\left[\frac{1}{2}\left(\frac{\partial u_i^n}{\partial x_j} + \frac{\partial u_i^*}{\partial x_j}\right) + \left(\frac{\partial u_j^n}{\partial x_i}\right)\right]_{\text{face}}$$

In the above expressions, the velocities at the 'face' are obtained by using arithmetic averages of the neighboring cvs attached to the face. For the viscous terms, the velocity gradients in the direction of the momentum component are obtained implicitly using Crank-Nicholson scheme. A centered discretization scheme is used for spatial gradients. Evaluation of the pressure gradients at the cv centers is explained below.

Step 4: Solve the variable coefficient Poisson equation for pressure:

$$\frac{1}{\Delta t} \sum_{\text{faces of cv}} u_N^* A_{\text{face}} = \sum_{\text{faces of cv}} \frac{1}{\rho_{\text{face}}^{n+1/2}} A_{\text{face}} \frac{\delta p}{\delta N}^{n+1/2}, \tag{13}$$

where ρ_{face} is obtained using arithmetic averages of density in the neighboring cvs. The face-normal velocity u_N^* and the face-normal pressure gradient are obtained as:

$$u_N^* = \frac{1}{2}(u_{i,\text{nbr}}^* + u_{i,\text{cv}}^*)N_{i,\text{face}}$$

$$\frac{\delta p}{\delta N}^{n+1/2} = \frac{p_{\text{nbr}}^{n+1/2} - p_{\text{cv}}^{n+1/2}}{|\mathbf{s}_{\text{cv,nbr}}|}$$

where nbr represents neighboring cv associated with the $face$ of the cv, and $|\mathbf{s}_{\text{cv,nbr}}|$ is the distance between the two cvs. The variable-coefficient pressure equation is solved using a Bi-Conjugate gradient algorithm by van der Vorst (2003).

Step 5: Reconstruct the pressure gradient at the cv centers using density and face-area weighting first proposed by Ham and Young (2003)

$$\frac{1}{\rho_{cv}^{n+1/2}} \frac{\delta p}{\delta x_i}^{n+1/2} =$$

$$\frac{\sum_{\text{faces of cv}} \frac{1}{\rho_{\text{face}}^{n+1/2}} \frac{\delta p}{\delta N}^{n+1/2} \cdot \vec{i} |N_{i,\text{face}} A_{\text{face}}|}{\sum_{\text{faces of cv}} |N_{i,\text{face}} A_{\text{face}}|} \tag{14}$$

Step 6: Update the cv-center and face-normal velocities to satisfy the incompressibility constraint:

$$\widehat{u}_{i,\text{cv}} = u_{i,\text{cv}}^* - \Delta t \frac{\delta p_{\text{cv}}^{n+1/2}}{\delta x_i} \tag{15}$$

$$\widehat{u}_N = u_N^* - \Delta t \frac{\delta p^{n+1/2}}{\delta N} \tag{16}$$

The face-normal velocity field $\widehat{u}_N$ will satisfy the incompressibility constraint, however, the cv-based velocity may not satisfy the rigid-body constraint inside the particle region. Note that in the absence of any rigid body, $\rho = \rho_F$ throughout the domain, and the algorithm reduces to the standard fractional step scheme for single-phase, incompressible flow. The above velocity field will then be denoted as $u_{i,\text{cv}}^{n+1}$. In the presence of rigid bodies, the following steps are performed to enforce the rigidity constraint within the particle domain.

Step 7: First interpolate the velocity field $\widehat{u}_{i,\text{cv}}$ from the grid cvs to the material volume centroids to obtain $\widehat{U}_{i,M}$ using the kernel interpolation outlined in Apte et al. (2009). Solve for the translational and rotational velocity fields

$$\mathcal{M}_P \mathbf{U}_P^T = \sum_{M=1}^{N} V_M \rho_M \mathbf{U}_M \tag{17}$$

$$\mathcal{I}_P \mathbf{\Omega}_P = \sum_{M=1}^{N} \rho_M V_M (\mathbf{r} \times \mathbf{U}_M), \tag{18}$$

where subscripts P and M denote the particle and the material volume centroids respectively, V_M is the volume and ρ_M the density of each material volume, $\mathcal{M}_P = \sum_{M=1}^{N} \rho_M V_M$ is the total mass of the particle, $\mathcal{I}_P$ is the moment of inertia of the particle about the coordinate axes fixed to the particle centroid, and $\mathbf{r}$ is the position vector of a point within the particle region with respect to the particle centroid.. The moment of inertia is given as

$$\mathcal{I}_P = \sum_{M=1}^{N} \rho_M V_M \left[(\mathbf{r} \cdot \mathbf{r})\mathbf{I} - \mathbf{r} \otimes \mathbf{r} \right], \tag{19}$$

where $\mathbf{I}$ represents the identity matrix. The rigid body motion is then obtained as:

$$\mathbf{U}_M^{RBM} = \mathbf{U}_M^T + \mathbf{\Omega}_P \times (\mathbf{X}_M - \mathbf{X}_P). \tag{20}$$

Step 8: Compute the rigid-body constraint force and correct the velocity field to satisfy this constraint within the particle region.

$$\mathrm{F}_{i,M}^{n+1} = -\frac{(U_{i,M} - U_{i,M}^{RBM,n+1})}{\Delta t}. \tag{21}$$

The force on the grid control volumes ($f_{i,\text{cv}}$) is obtained from $\mathrm{F}_{i,M}$ through a consistent interpolation scheme scheme as presented by Apte et al. (2009). The velocity field inside the particle region is then modified as:

$$u_{i,\text{cv}}^{n+1} = \widehat{u}_{i,\text{cv}} + \Delta t f_{i,\text{cv}}^{n+1}. \tag{22}$$

Numerical Test Cases

The above numerical algorithm is implemented in a parallel, finite volume framework and validated for a number of test cases: (i) flow over a fixed sphere and hydrofoil, (ii) particle subjected to constant acceleration for varying fluid-particle density ratios, and (iii) freely falling/rising particles at low and high density ratios. Finally, we simulate interactions of a buoyant sphere with a stationary Gaussian vortex at different density ratios.

Table 1: Drag coefficient C_d for flow over a sphere at different Reynolds number

Study	Re_p					
	20	50	100	150	300	350
Current	**2.633**	**1.550**	**1.101**	**0.907**	**0.686**	**0.649**
Mittal (1999)	-	1.57	1.09	-	-	0.62
Mittal et al. (2008)	-	-	1.08	0.88	0.68	0.63
Clift et al. (1978)	2.61	1.57	1.09	0.89	0.684	0.644
Johnson and Patel (1999)	-	1.57	1.08	0.9	0.629	-
Marella et al. (2005)	-	1.56	1.06	0.85	0.621	-
Kim et al. (2001)	-	-	1.087	-	0.657	-
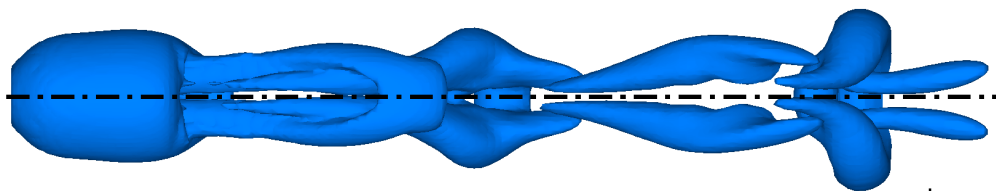
Figure 2: Iso-surface of $\lambda = 0.008$ for flow over a stationary sphere at $Re_p = 350$ in the xz plane. The dash-dotted line shows the symmetry axis of the structure in this plane.

Flow over a Sphere   To evaluate the accuracy of the algorithm for three-dimensional configurations, flow over a fixed sphere at different Reynolds number is first evaluated and compared with published data. A sphere of diameter $d = 1.10\ mm$ is placed in a domain of $15d \times 15d \times 15d$. The sphere is located at $x = 5d$ and $y = z = 7.5d$. The grid used is $128 \times 128 \times 128$. The grid is non-uniform but it is refined and uniform around the sphere forming a patch of $1.5d \times 1.5d \times 1.5d$. There are approximately 26 grid points along a diameter of the sphere. For comparison Mittal et al. (2008) used a domain of $16d \times 15d \times 15d$ and a grid of $192 \times 120 \times 120$ for their highest Reynolds number of 350 and Marella et al. (2005) employed a $130 \times 110 \times 110$ mesh on a $16d \times 15d \times 15d$ domain. The fluid properties are $\rho = 1\ kg/m^3$ and the viscosity $\mu = 10^{-5}\ kg/m.s$. The x direction is slightly moved towards the inlet in order to increase the size of the domain in the wake. Also the density of grid-points is increased in the wake of the sphere in order to properly resolve the flow. Table 1 compares the predicted drag coefficients with other published data showing very good predictions.

Figure 2 shows the vortical structure represented by the eigenvalues of the velocity gradient tensor λ in the xz plane for $Re_p = 350$. Qualitatively the plots show very similar structures as shown by Mittal (1999). This snapshot shows the vortex ring in the near wake of the sphere. Another important feature is the symmetry axis shown in the xz plane which has been observed experimentally.

NACA 0008 Hydrofoil   The computational solution of flow over a stationary NACA 0008 hydrofoil is presented to show the applicability of the present approach to irregular geometries. The thin hydrofoil geometry is challenging for this method because of the small radius at the foil's leading edge and the sharp tip at the trailing edge. These features lead to distinct lift and drag characteristics associated with the geometry, and it is important for any flow solver to properly resolve them.

A two dimensional flow is assumed, and a block type Cartesian grid with periodic boundaries in the spanwise direction is generated using $504 \times 200 \times 4$ grid points in the streamwise, crossstream, and spanwise directions respectively. The domain itself is $13c$ long in the streamwise direction and $8c$ wide in the crossstream direction, where c is the hydrofoil chord length. The grid around the hydrofoil and in the near wake is uniform and cubic with spacing equal to $c/400$. By comparison, Mittal et al. (2008) used 926×211 grid points in the x and y directions for a cartesian grid based immersed boundary solution. Kunz and Kroo (2001) used a body fitted C-grid and a two dimensional solver with 256×64 grid points in the hydrofoil plane. The chord based Reynolds number, $Re_c = \rho U_\infty c/\mu$, is fixed at 2000. Two angles of attack $\alpha = 0^o$ and $\alpha = 4^o$ are used. The simulations are run for 15 non dimensional time units, $\frac{tU_\infty}{c}$. Relevant computational parameters are summarized in table 2.

At this Reynolds number, the flow is laminar, two-dimensional and steady. Figure 3 shows the contours of

Table 2: Parameters for NACA0008 hydrofoil.

Re_c	α	L_x	L_y	N_x	N_y	N_z	$\frac{c}{\Delta_x}$
2,000	$0^o, 4^o$	13c	8c	504	200	4	400

Table 3: Comparison of steady state drag and lift coefficients with other 2D computational results

Study	$\alpha = 0^o$	$\alpha = 4^o$	
	C_D	C_D	C_L
Present Results	0.078	0.083	0.270
Mittal et al. (2008)	0.078	0.081	0.273
Kunz and Kroo (2001)	0.076	0.080	0.272

vorticity for $\alpha = 0^o$ and 4° after the flow has reached steady state. At $\alpha = 0$, the flow is symmetric, and the wake is quite narrow. At $\alpha = 4$, the wake is widened, and separation is indicated on the suction side by detachment of the high vorticity region from the surface.

(a) $\alpha = 0^o$

(b) $\alpha = 4^o$
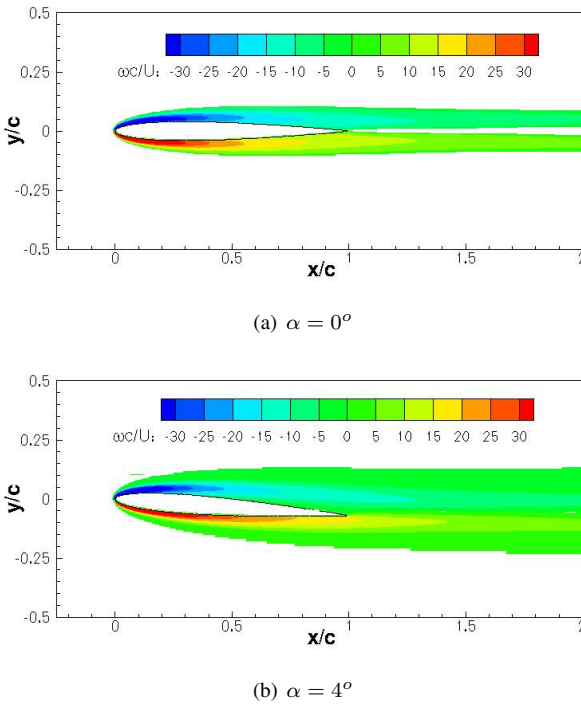
Figure 3: Contours of vorticity (out of the page) for flow around a NACA 0008 hydrofoil at Re = 2,000

The lift and drag coefficients for the hydrofoil are given as:

$$C_D = \frac{F_D}{\frac{1}{2}\rho U_\infty^2}; \quad C_L = \frac{F_L}{\frac{1}{2}\rho U_\infty^2} \qquad (23)$$

The steady state values of C_L and C_D are taken after 15 time units and are compared to the published data in table 3. The present steady state values are in good agreement with the previous computational studies.

Sphere subjected to uniform acceleration To test the stability of the numerical algorithm for high density ratio between the particle and the fluid, we consider motion of a spherical particle subjected to uniform acceleration (**a**) in a closed box. If viscous and gravitational

effects are negligible, this case has a simple analytical solution of $\mathbf{u} = \mathbf{u}_0 + \mathbf{a}t$; where $\mathbf{u}$ and $\mathbf{u}_0$ are the instantaneous and initial velocity fields, respectively and t is time. Initially, a particle of diameter $5\ mm$ is placed at the center of a cubic box of $3\ cm$. Uniform cubic grids of $100 \times 100 \times 100$ grid points is used. The fluid density is set to $1\ \text{kg/m}^3$ and the viscosity and gravitational acceleration are turned off. The particle starts from rest and is subjected to uniform acceleration of $(-40, -40, -40)\ m/s^2$. The particle density is varied over a wide range 10^3, 10^4 and 10^6 and the distance traveled by the particle is compared to the analytical solution of $S = |\mathbf{u}_0|t + 1/2|\mathbf{a}|t^2$. Figure 4 shows the temporal evolution of relative error in the distance traveled by the particle compared to the exact solution ($|\frac{S_{num} - S_{exact}}{S_{exact, t=0.01}}|$) over 1000 iterations with fixed time step of $10\ \mu s$. It is observed that the error remains small for high density ratios.
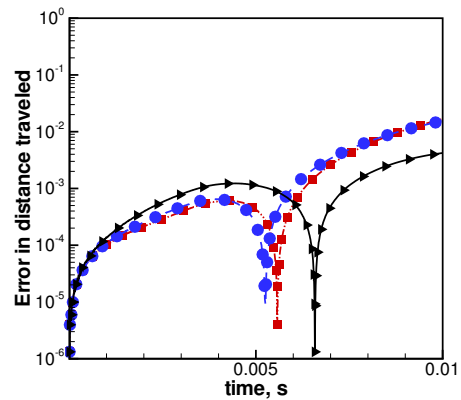
Figure 4: Temporal evolution of the relative error in distance traveled by the sphere under uniform acceleration: ▲ $\rho_p/\rho_f = 10^3$, ● $\rho_p/\rho_f = 10^4$, □ $\rho_p/\rho_f = 10^6$.

Sphere rising in inclined channel A lighter-than-fluid particle rising in an inclined channel is considered next. The simulation is conducted with a fluid density of $\rho_f = 1115\ kg/m^3$, a particle density of $\rho_p =$
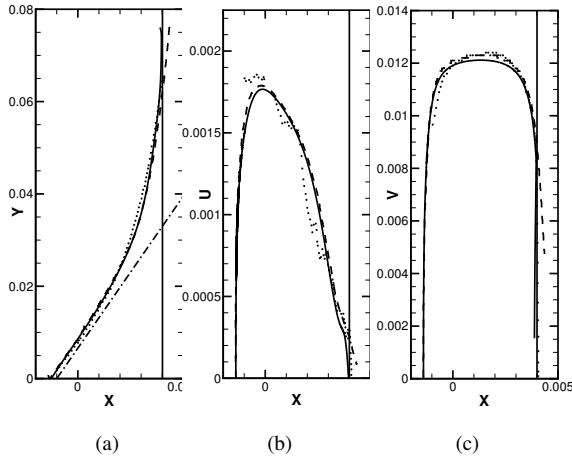
Figure 5: Comparison of experimental ● and numerical simulations − − − Lomholt et al. (2002) with the current simulation —. Figure 5(a) shows the particle trajectory inside the domain (the −.− line shows the initial trajectory due only to the effect of gravity), 5(b) the velocity of the particle in the lateral direction and 5(c) the velocity on the vertical direction. The particle position is expressed in $[m]$ and the velocities are expressed in $[m/s]$.

$1081\,kg/m^3$, and a fluid viscosity of $\nu = 3.125\,mm^2/s$. The Reynolds number Re_p^{Stokes} based on the Stokes settling velocity W is defined as :

$$Re_p^{Stokes} = \frac{2d_pW}{\nu} = \frac{4d_p^3}{9\nu^2}|\frac{\rho_p}{\rho_f} - 1|g \qquad (24)$$

where $g = 9.82\,m/s^2$ is the gravitational acceleration, and $d_p = 2\,mm$ is the diameter of the particle. The channel is inclined at an angle of $8.23°$ with the vertical. This is simulated by adding components of gravitational forces in the horizontal and vertical directions.

The computational domain consists of a rectangular box with dimensions $10\,mm$ in the x direction, $80\,mm$ in the y direction and $40\,mm$ in the z direction. The grid is Cartesian and uniform over the domain with $40 \times 320 \times 160$ grid points, respectively in the x, y and z directions so that $\Delta = 0.25 \times 10^{-3}\,m$. The particle is injected at $x = -1.4\,mm$, $y = -1.0\,mm$ and $z = 20.0\,mm$. Simulation results for a Reynolds number of $Re_p^{Stokes} = 13.6$ are compared with experimental and numerical data from Lomholt et al. (2002). As illustrated in Figure 5, the numerical simulation exhibits excellent agreement with both experimental and numerical results. Buoyancy forces cause the particle to rise and travel alongside the right wall of the domain. Ultimately, the particle follows the right wall without touching it, keeping a very thin lubrication layer between the particle and the wall.

Freely falling sphere We consider the problem of a single sphere falling under gravity in a closed container. The particle density is ($\rho_p = 1120\,kg/m^3$) and the diameter is (15 mm). The sphere is settling in a box of dimensions $10 \times 10 \times 16\,cm^3$. The particle is released at a height $H = 12\,cm$ from the bottom of the box. The boundaries of the box are treated as no-slip walls. The fluid propertiies are varied to obtain different Reynolds numbers based on the terminal velocity of the particle. The simulation conditions correspond to the experimental study by ten Cate et al. (2002). Table 4 provides detailed information about the parameters used in this test problem. We simulate the above cases on a fine uniform

Table 4: Parameters for freely falling sphere.

|	ρ_F (kg/m³)	μ_F (10^{-3}Ns/m²)	Re
#1	970	373	1.5
#2	965	212	4.1
#3	962	113	11.6
#4	960	58	31.9

grid of $100 \times 100 \times 160$ points with a grid resolution of $\Delta = 1$ mm. This provides around 15 grid points inside the particle domain. The material volumes are cubical with $\frac{\Delta}{\Delta_M} = 5$, where Δ_M is the size of the material volume. Accordingly, there are around 75 material volumes along the diameter of the spherical particle in each direction. A uniform time-step ($\Delta t = 0.5$ ms) is used for all cases.

Figures 6a-b show the comparison of the time evolution of particle settling velocity and position at different times obtained from the numerical simulations with the experimental data by ten Cate et al. (2002). The simulation predictions for both the particle velocity and the particle position show good agreement with the experimental data. The slowing of the particle towards the end of the simulation are to due to the presence of the bottom wall.

Falling sphere with high density ratio To test the accuracy of the numerical algorithm for high density ratio between the particle and the fluid, we consider the same problem of falling sphere, except vary the density of the particle keeping the fluid density fixed at $\rho_f = 1\,kg/m^3$. The particle density (ρ_p) is varied over a wide range 10, 100, 500 and 1000. To keep the terminal velocity of the particle small the viscosity of the fluid is set at $0.06\,[kg/m.s]$. The diameter of the particle, the domain size, computational grid and release point at same as that of the above case.

Mordant and Pinton (2000) performed experiments on freely falling spherical particles in a large water tank
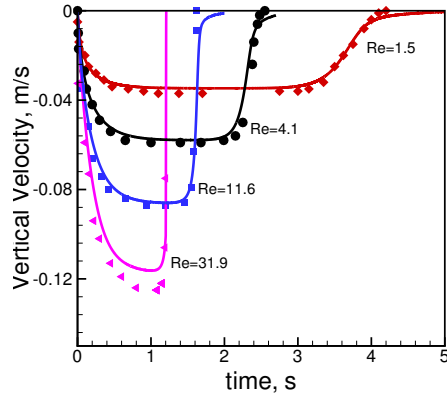
(a) Fall Velocity
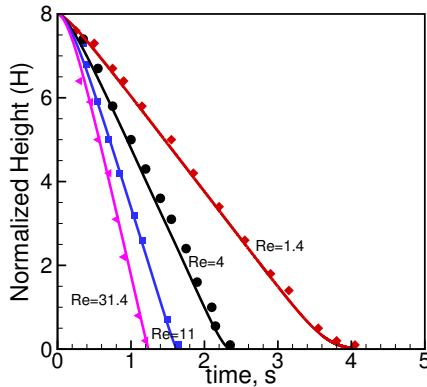
(b) Normalized Height

Figure 6: Comparison with the experimental data of the sphere fall velocity and the normalized height from the bottom wall for different Reynolds numbers: (Symbols: experiment by ten Cate et al. (2002), lines: present simulation) Here $H = \frac{h - 0.5 d_P}{d_P}$ where h is the height of the sphere center from the bottom wall and d_P is the particle diameter.
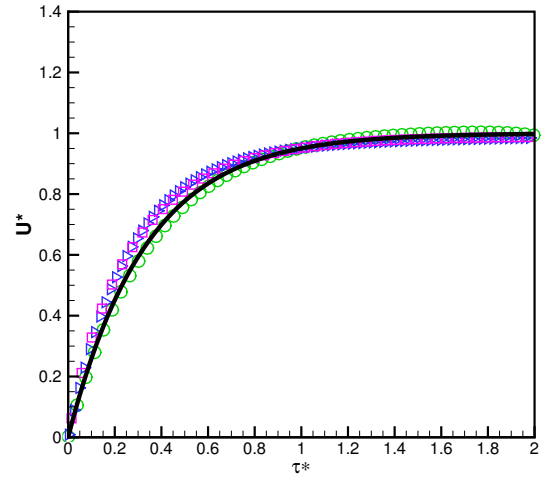
Figure 7: Temporal evolution of a spherical particle rising in a water column: $U^* = U/U_{terminal}$, $\tau^* = t/\tau_{95}$: solid line by Mordant and Pinton (2000); $\rho_p/\rho_f = 500$ (○); $\rho_p/\rho_f = 100$ (□); $\rho_p/\rho_f = 10$ (▷) present simulations.

for various density ratios (maximum density ratio considered was $\rho_p/\rho_f = 14.6$). They showed that for small particles falling in a large tank (that is, for small values of the ratio of particle diameter to tank width $d_p/L \sim 0.005$) the temporal evolution of the particle velocity can be well predicted by the the curve:

$$U^* = 1 - \exp\left(-\frac{3t}{\tau_{95}}\right), \quad (25)$$

where U^* is the velocity of the particle normalized by its terminal velocity, τ_{95} is the time it takes for the sphere to reach 95% of its terminal velocity, and t is time. We compare the temporal evolution of the rising spherical particle to this curve in Figure 7. The temporal evolution of the particle velocity is qualitatively similar to the exponential curve. The domain size in simulations is small ($d_p/L = 0.15$) and thus wall effects become important. This test case confirms the stability of the numerical solver when applied to large-density ratio fluid-particle systems.

Buoyant sphere in a Gaussian vortex

We now consider the entrainment of a single buoyant sphere in a stationary Gaussian vortex as shown in figure 8(a). The buoyant sphere is released in the vicinity of the vortex with core radius, r_c and initial circulation, Γ_0. With sufficient vortex strength, the sphere gets entrained into the vortex after circling around several times

9

and reaching a settling location with relative coordinates r_s, θ_s measured from the vortex center. For the Gaussian vortex, there is no radial velocity component, and the the tangential velocity is expressed as

$$u_\theta(r) = \frac{\Gamma_0}{2\pi r} \left(1 - e^{-\eta_1 (r/r_c)^2} \right) \qquad (26)$$

The vorticity and maximum tangential velocity (occurs at $r = r_c$) are given by

$$\omega(r) = \frac{\Gamma_0 \eta_1}{\pi r_c^2} e^{-\eta_1 (r/r_c)^2}; \quad u_c = \eta_2 \frac{\Gamma_0}{2\pi r_c}, \qquad (27)$$

where η_1 and η_2 are constants. This flow has been used previously by Oweis et al. (2005), as a model for wingtip vortices in their study of bubble capture and cavitation inception. Variables relevant for the setup of this test case are summarized in table 5. The domain size is approximately $7\,r_c \times 7\,r_c \times 0.4\,r_c$. A slip condition is imposed at boundaries in the X and Y directions, and the domain is periodic in the Z direction. The Cartesian grid is refined in the area of the vortex core with a cubic spacing of $\Delta_{core} = 0.1\ mm$ and has $450 \times 450 \times 50$ grid points in the X, Y and Z directions. The velocity field of equation 26 is applied as an initial condition everywhere in the domain, creating a clockwise vortex with initial strength $\Gamma_0 = 0.04 m^2 s^{-1}$. During the first timestep, a single, $1.1\ mm$ diameter spherical particle is released at $r = r_c$, $\theta = 0$. We assume typical properties of water for the fluid phase and simulate 3 different particle densities corresponding to $\rho_f/\rho_p =$ 100, 500, and 1000. In each case, the simulation is advanced using a timestep of $\Delta t = 50\ \mu s$ up to a time of $1\ s$. Figure 8(b) shows the entrainment trajectories of

Table 5: Parameters for the Gaussian vortex case.

$r_c\ [mm]$	11.45
η_1	1.27
η_2	0.715
$L_x,\ L_y\ L_z\ [mm]$	80,80,5
$\Delta_{core}\ [mm]$	0.1
N_{grid}	$425 \times 425 \times 50$
$\Gamma_0\ [m^2/s]$	0.04
$d_p\ [m]$	1.1
$\rho_f\ [kg/m^3]$	1,000
$\rho_p\ [kg/m^3]$	1, 2, 10
$\mu_f\ [kg/m.s]$	0.001

the spheres for each density ratio considered. Because of the high density ratios, the spheres do not follow the fluid streamlines and instead are attracted toward the upper right hand side of the inner core. This is due to the lift and added mass effects effects similarly observed

Table 6: Average settling coordinates of the sphere in the vortex core as shown in figure 8(a)

| Density Ratio	r_s/r_c	$\theta_s\ [rad]$
$\rho_f/\rho_p = 100$	0.30	0.005
$\rho_f/\rho_p = 500$	0.45	-0.065
$\rho_f/\rho_p = 1,000$	0.57	-0.106

by Mazzitelli et al. (2003); Climent et al. (2007) for bubbles entrained in vortical structures. As density ratio and relative buoyancy force are increased, a more direct path is taken to the settling location by the sphere. The settling coordinates are tabulated in table 6 for each case. With increased density ratio, the spheres reach equilibrium at a larger radius and more negative angle from the horizontal. For ρ_f/ρ_p equal to 100 and 500, there is little relative motion of the sphere once it becomes entrained. At $\rho_f/\rho_p = 1000$, a much different dynamic exists because the sphere does not stay in one location. Rather it circles a point centered at $(r_s/r_c,\ \theta_s) = (0.57, -0.106)$. This motion causes a strong and highly unsteady wake to develop behind the sphere as is shown in figure 9. Strong vortical structures are periodically shed from the sphere, and advected clockwise around the vortex core back to the sphere.

Conclusion

A numerical formulation for fully resolved simulations of freely moving rigid particles for a wide range of fluid-particle density ratios is developed based on a fictitious domain method. In this approach, the entire computational domain is first treated as a fluid of varying density corresponding to the fluid or particle densities in their respective regions. The incompressibility and rigidity constraints are applied to the fluid and particle regions, respectively, by using a fractional step algorithm. The momentum equations are recast to avoid computations of density variations across the fluid-particle interface. The resultant equations are discretized using symmetric central differences in space and time. Use of consistent interpolations between the particle material volumes and the background grid and parallel implementation of the algorithm facilitates accurate and efficient simulations of large number of particles. Implementation of this approach in finite-volume, co-located grid based numerical solver is presented. The numerical approach is applied to simulate flow over a fixed immersed objects (sphere and NACA0008 hydrofoil) at different Reynolds numbers, freely falling/rising spheres for a wide range of density ratios and compared with published experimental or numerical results to show good agreement. Finally, the approach was applied to simulate freely moving buoyant spheres in a stationary Gaussian vortex for
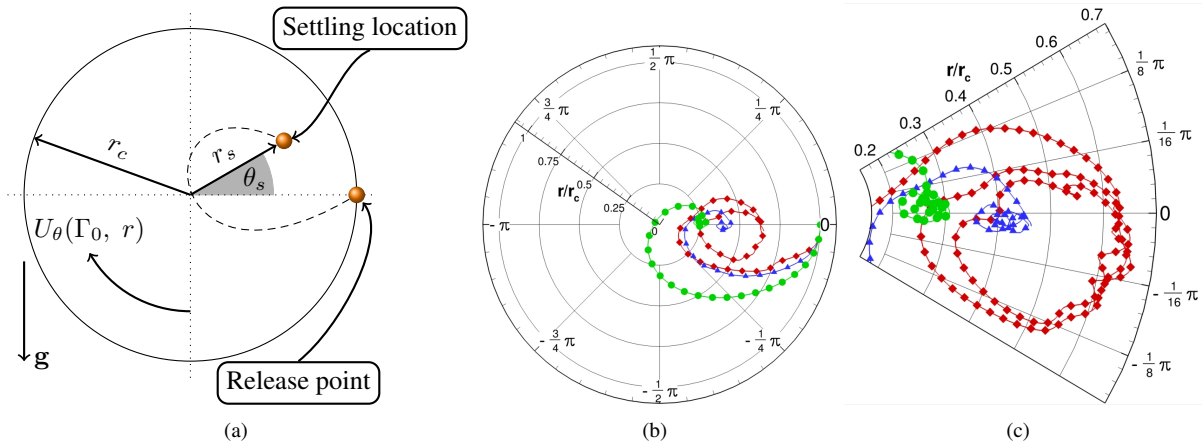
Figure 8: Entrainment of a buoyant sphere by a Gaussian vortex of core radius r_c: (a) Problem schematic, showing the definition of the settling coordinates (r_s, θ_s), (b) Entrainment trajectories for the three cases simulated, (c) The motion of the sphere at the settling location. ● $\rho_f/\rho_p = 100$, ▲ $\rho_f/\rho_p = 500$, ♦ $\rho_f/\rho_p = 1000$

(a) $t = 0$

(b) $t = 0.05s$

(c) $t = 0.1s$

(d) $t = 0.5s$

(e) $t = 0.6s$

(f) $t = 0.7s$
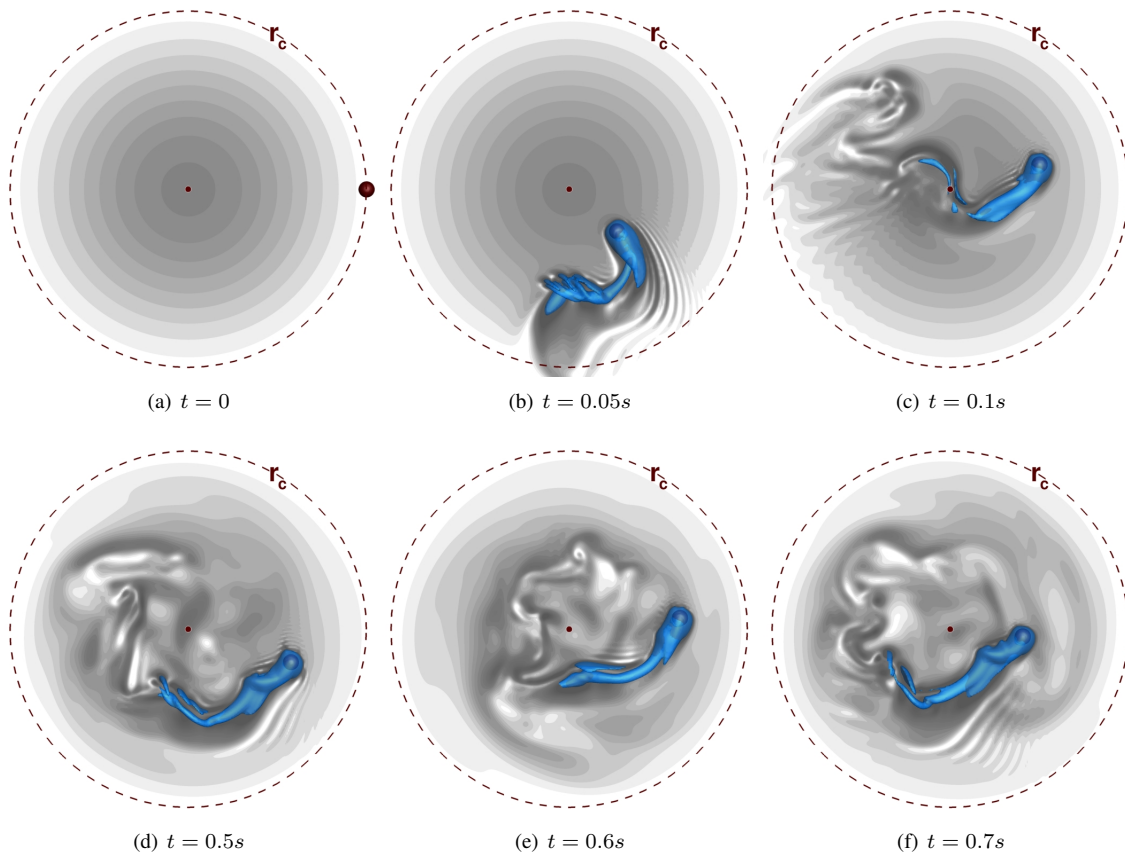
Figure 9: Snapshots of fluid vorticity magnitude in the vortex core for the high density ratio case ($\rho_f/\rho_p = 1000$) Contours are from 20 to 250 m^2/s. Isosurface of 350 m^2/s is also shown.

a range of density ratios to investigate the ability of the solver to capture lift and added-mass effects on lighter-than fluid particles in vortical flows. For large vortex strengths, the lighter-than fluid particles are attracted towards the core of the vortex and settle further away from the center in the presence of gravity as expected.

Acknowledgements

References

S.V. Apte, M. Martin, and N.A. Patankar. A numerical method for fully resolved simulation (FRS) of rigid particle-flow interactions in complex flows. *Journal of Computational Physics*, 228(8):2712–2738, 2009.

M. Bussmann, DB Kothe, and JM Sicilian. Modeling high density ratio incompressible interfacial flows. In *Proc. FEDSM*, volume 2, pages 2002–31125, 2002.

R. Clift, J.R. Grace, and M.E. Weber. *Bubbles, drops, and particles*. Academic Press, New York, 1978.

E. Climent, M. Simonnet, and J. Magnaudet. Preferential accumulation of bubbles in Couette-Taylor flow patterns. *Physics of Fluids*, 19:083301, 2007.

Z.G. Feng and E.E. Michaelides. Proteus: a direct forcing method in the simulations of particulate flows. *Journal of Computational Physics*, 202(1):20–51, 2005.

R. Glowinski, TW Pan, TI Hesla, DD Joseph, and J. Periaux. A fictitious domain approach to the direct numerical simulation of incompressible viscous flow past moving rigid bodies- application to particulate flow. *Journal of Computational Physics*, 169(2):363–426, 2001.

F. Ham and YN. Young. A Cartesian Adaptive Level Set Method for Two-Phase Flows. *Annu. Research Briefs, 2003: Center for Turbulence Research*, 2003.

TA Johnson and VC Patel. Flow past a sphere up to a reynolds number of 300. *Journal of Fluid Mechanics*, 378:19–70, 1999.

D. Kim and H. Choi. A second-order time-accurate finite volume method for unsteady incompressible flow on hybrid unstructured grids. *Journal of Computational Physics*, 162(2):411–428, 2000.

D. Kim and H. Choi. Immersed boundary method for flow around an arbitrarily moving body. *Journal of Computational Physics*, 212(2):662–680, 2006.

J. Kim, D. Kim, and H. Choi. An immersed-boundary finite-volume method for simulations of flow in complex geometries. *Journal of Computational Physics*, 171(1): 132–150, 2001.

PJ Kunz and I. Kroo. Analysis and design of airfoils for use at ultra-low Reynolds numbers. *Progress in Astronautics and Aeronautics*, 195:35–60, 2001.

A.J.C. Ladd and R. Verberg. Lattice-Boltzmann simulations of particle-fluid suspensions. *J. Statist. Phys.*, 104: 1191–1251, 2001.

S. Lomholt, B. Stenum, and MR Maxey. Experimental verification of the force coupling method for particulate flows. *International Journal of Multiphase Flow*, 28(2): 225–246, 2002.

K. Mahesh, G. Constantinescu, S. Apte, G. Iaccarino, F. Ham, and P. Moin. Large-Eddy Simulation of Reacting Turbulent Flows in Complex Geometries. *Journal of Applied Mechanics*, 73:374, 2006.

S. Marella, S. Krishnan, H. Liu, and HS Udaykumar. Sharp interface cartesian grid method i: An easily implemented technique for 3d moving boundary computations. *Journal of Computational Physics*, 210(1):1–31, 2005.

I.M. Mazzitelli, D. Lohse, and F. Toschi. On the relevance of the lift force in bubbly turbulence. *Journal of Fluid Mechanics*, 488:283–313, 2003.

R. Mittal. A fourier-chebyshev spectral collocation method for simulating flow past spheres and spheroids. *International Journal for Numerical Methods in Fluids*, 30(7):921–937, 1999.

R. Mittal and G. Iaccarino. Immersed boundary methods. *Annual Review of Fluid Mechanics*, 37(1):239–261, 2005.

R. Mittal, H. Dong, M. Bozkurttas, FM Najjar, A. Vargas, and A. Von Loebbecke. A versatile sharp interface immersed boundary method for incompressible flows with complex boundaries. *Journal of computational physics*, 227(10):4825–4852, 2008.

N. Mordant and J.F. Pinton. Velocity measurement of a settling sphere. *The European Physical Journal B*, 18 (2):343–352, 2000.

S. Osher and R.P. Fedkiw. *Level set methods and dynamic implicit surfaces*. Springer Verlag, 2003.

S. Osher and J.A. Sethian. Fronts propagating with curvature-dependent speed: algorithms based on Hamilton-Jacobi formulations. *Journal of computational physics*, 79(1):12–49, 1988.

GF Oweis, IE van der Hout, C. Iyer, G. Tryggvason, and SL Ceccio. Capture and inception of bubbles near line vortices. *Physics of Fluids*, 17:022105, 2005.

NA Patankar, P. Singh, DD Joseph, R. Glowinski, and T.W. Pan. A new formulation of the distributed Lagrange multiplier/fictitious domain method for particulate flows. *International Journal of Multiphase Flow*, 26(9):1509–1524, 2000.

C.S. Peskin. The immersed boundary method. *Acta Numerica*, 11:479–517, 2003.

M. Raessi. A level set based method for calculating flux densities in two-phase flows. *Annual Research Briefs*, pages 467–478, 2008.

AM Roma, CS Peskin, and MJ Berger. An Adaptive Version of the Immersed Boundary Method. *Journal of Computational Physics*, 153(2):509–534, 1999.

M. Rudman. A volume-tracking method for incompressible multifluid flows with large density variations. *International Journal for Numerical Methods in Fluids*, 28 (2):357–378, 1998.

N. Sharma and N.A. Patankar. A fast computation technique for the direct numerical simulation of rigid particulate flows. *Journal of Computational Physics*, 205(2): 439–457, 2005.

K. Taira and T. Colonius. The immersed boundary method: A projection approach. *Journal of Computational Physics*, 225(2):2118–2137, 2007.

A. ten Cate, CH Nieuwstad, JJ Derksen, and HEA Van den Akker. Particle imaging velocimetry experiments and lattice-Boltzmann simulations on a single sphere settling under gravity. *Physics of Fluids*, 14:4012, 2002.

M. Uhlmann. An immersed boundary method with direct forcing for the simulation of particulate flows. *Journal of Computational Physics*, 209(2):448–476, 2005.

HA van der Vorst. *Iterative Krylov Methods for Large Linear Systems*. Cambridge University Press, 2003.

C. Veeramani, PD Minev, and K. Nandakumar. A fictitious domain formulation for flows with rigid particles: A non-Lagrange multiplier version. *Journal of Computational Physics*, 224(2):867–879, 2007.

Z. Zhang and A. Prosperetti. A second-order method for three-dimensional particle simulation. *Journal of Computational Physics*, 210(1):292–324, 2005.